Influence of Electrode Potential on Oxygen Mobility Probed by Polarized Isotopic Exchange in Solid Oxide Electrolyser Cells: Insights for Electro-Assisted Oxidation Reactions

Alexandre Manon, Alexandre Nau, Thomas Belin, Arnaud Mazurier, Jean Marc Bassat, Nicolas Bion, Clément Comminges

WILEY VCH

RESEARCH ARTICLE

Influence of Electrode Potential on Oxygen Mobility Probed by Polarized Isotopic Exchange in Solid Oxide Electrolyser Cells: Insights for Electro-Assisted Oxidation Reactions

Alexandre Manon[a], Alexandre Nau[a], Thomas Belin[a], Arnaud Mazurier[a], Jean Marc Bassat[b], Nicolas Bion[a] and Clément Comminges*[a]

[a] Dr. A Manon, Dr. A. Nau, Dr. T. Belin, Dr. A. Mazurier, Dr. N. Bion, Dr. C. Comminges
Institut de Chimie des Milieux et Matériaux de Poitiers (IC2MP)
Université de Poitiers, CNRS
4 rue Michel Brunet, TSA 51106, F86073, Poitiers cedex 9, France
E-mail: clement.comminges@univ-poitiers.fr

[b] Dr. J.M. Bassat
Institut de Chimie de la Matière Condensée de Bordeaux (ICMCB)
Université de Bordeaux, CNRS
87 Avenue du Dr. Albert Schweitzer, F33600, Pessac, France

Supporting information for this article is given via a link at the end of the document.

Abstract: Oxygen mobility was studied by oxygen isotopic exchange on three electrodes used in Solid Oxide Electrolyser Cells under polarization ($La_{0.8}Sr_{0.2}MnO_3$ (LSM), $La_{0.6}Sr_{0.4}Co_{0.2}Fe_{0.8}O_{3-\delta}$ (LSCF) and $La_2NiO_{4+\delta}$ (LNO)). The rate of the surface and the bulk mechanisms for oxygen mobility is depending on the type of conductivity (electronic conduction or mixed ionic and electronic conductivity). It is shown that a one oxygen atom exchange is dominant for the surface path whereas a two oxygen atoms mechanism dominates for the bulk path. The rate constant for the bulk path is much higher than the one for the surface path by two orders of magnitude. Additionally, polarized oxygen isotopic exchange revealed that electrode overvoltage increases significantly the rate constant for the surface path, whereas its impact on the bulk path is negligible.

Introduction

Coupling catalytic oxidation reactions with gas phase electrocatalysis by employing Solid Oxide Electrolyser Cells (SOEC) is a topic of raising interest. Indeed, SOEC systems are investigated for decades for high temperature water electrolysis (HTE) to produce hydrogen [1] or syngas (via CO_2 / H_2O co-electrolysis) [2] at the cathode. In these systems, the anodic reaction consists of releasing oxygen gas *via* the oxygen evolution reaction (OER). Attempts to valorise this oxygen through coupled catalytic oxidation reactions at the anode of the SOEC have been realized to generate valuable molecules. By introducing CH_4 in the anodic chamber, valuable CH_4 oxidation products can be obtained (syngas by partial oxidation of methane or ethylene *via* oxidative coupling of methane) [3], while undesirable CO_2 resulting from CH_4 combustion is to be avoided [4]. To perform these catalytically assisted electrolyses, one must develop anodic electrocatalysts that fulfils the classical prerequisites in electrochemistry (electronic conduction, O^{2-} ionic conduction) as well as in gas phase catalysis (porosity, specific surface area, active sites for CH_4 adsorption, C-H bond activation, oxygen surface / bulk diffusion…). The control of the oxygen mobility is therefore crucial for the development of this technology. Reference materials used as anodes in SOEC are classically doped perovskites [5] or Ruddlesden-Popper phases [6]. There is therefore a great challenge both in the material development as well as in the understanding of oxygen mobility in these materials. Among the fundamental questions that can be raised, the effect of the electrode potential on the oxygen mobility is particularly relevant. Only few studies related to oxygen *operando* isotopic exchange with a control of the electrode potential have been performed. Sobyanin *et al.* performed homomolecular oxygen isotope exchange on a Pt/10-YSZ/Pt electrochemical cell at 500°C and concluded that the electrode polarization had not effect on the oxygen homomolecular exchange rate with respect to its open circuit voltage. [7] Wachsman *et al.* developed another strategy that enables the possibility of performing Polarized Oxygen Isotopic Exchange (POIE) directly on catalytic powders. They investigated the influence of a cathodic polarization on the oxygen surface exchange coefficient (k*) of several catalysts (LSM, LSCF, LSC and LSF) and concluded that k* is greatly increasing with the applied overpotential (η). This study is confirming the findings of Hopper *et al.* which investigated epitaxial thin film heterostructures of LSCF/GDC/YSZ with *in situ* synchrotron X-ray diffraction. [8]

We recently developed the polarized isotopic exchange method that enables the possibility to perform Oxygen Isotopic Exchange (OIE) experiments *in situ* on symmetrical cells and to identify the rate determining step by evaluating the kinetic constant dependency on the applied electrode potential [9]. The goal of this study is to understand the influence of the electrode potential on the oxygen mobility on three different oxide materials classically used as oxygen electrodes in SOFC or SOEC cells:

i) $La_{0.8}Sr_{0.2}MnO_3$ (LSM), a perovskite with partially filled band considered as electronic conductor [10]. Due to its very poor oxygen ionic conductivity (D_{bulk} = $3.1.10^{-16}$ $cm^2.s^{-1}$ at 700°C) [11], active sites for oxygen reduction and incorporation are located at the triple phase boundary (TPB) [12], although at high overpotential

oxygen ions can diffuse in the bulk oxide to reach the LSM/YSZ interphase. [13]

ii) $La_{0.6}Sr_{0.4}Co_{0.2}Fe_{0.8}O_{3-\delta}$ (LSCF), an oxygen deficient perovskite with a band gap, considered as a p-type semi-conductor and possessing a Mixed Ionic and Electronic Conduction (MIEC) [10]. At temperatures below 600°C, the ionic conductivity is rather low and the classical TPB model applies, as for LSM. [14] Above 600°C, LSCF behaves as a MIEC and the oxygen reduction reaction (ORR) is stimulated by the formation of oxygen vacancies in the oxide while increasing the electrode overpotential. Interestingly, it has been shown on LSCF epitaxial thin films [8] as well as on LSCF polarized powder [15] that increasing the electrode overvoltage (cathodic or anodic) induces a significant increase in the surface exchange coefficient (k*).

iii) $La_2NiO_{4+\delta}$ (LNO) is a material which belongs to the so-called Ruddlesden-Popper series $Ln_{n+1}Ni_nO_{3n+1}$ (here with Ln = La and n =1). [6a] This compound shows a K_2NiF_4 – type layered structure, with alternating $LnNiO_3$ perovskite layers and LnO rocksalt layers within which reside the additional interstitial oxygen atoms. This oxygen over stoichiometry is responsible of a large oxygen conductivity, which combined to reasonable p-type electronic conduction properties [16] leads to obtain an oxide with interesting MIEC properties. [17] More precisely, the oxygen conductivity mechanism is labelled as interstitially, because involving a push-pull mechanism between the interstitial and apical oxygens (being the last ones located in the perovskite layer). [18] Thanks to the stacking along the crystallographic c-axis of the structure, such MIEC properties are anisotropic, being the conductivities about 1000 times larger in the (a,b) plane compared to the stacking c-axis. [19] It is to note that the oxygen over-stoichiometry (+δ) is influenced by the temperature and the oxygen partial pressure [16, 20], such oxide "breathing" in a reversible way oxygen above a limit located at low temperature (around 400°C). In first approximation, a decrease of the over-stoichiometry diminishes the ionic conductivity [21] and electronic conductivity, as it lowers at the same time the hole concentration. [16, 20] It is generally accepted that dissociative adsorption of oxygen is the rate determining step for LNO electrodes. [22] Such kind of nickelates (also including Ln = Pr and Nd) are extensively studied as SOFC oxygen electrode materials. [23]

Results and Discussion

OIE on Powder Samples

Diffusion coefficients and rate constants for heteroexchange were calculated by fitting the curves of heterolytic exchange with O_2. As detailed by Klier *et al.* [24] and Muzykantov *et al.* [25], three types of isotope exchange were considered in this numerical approach:

(i) homomolecular exchange type (named r_0) with no participation of atoms from the solid (Equation 1):

$^{18}O_2 + {}^{16}O_2 \rightarrow 2{}^{16}O{}^{18}O$ (1)

(ii) heterolytic exchange (named r_1) between one atom from the gas phase and one atom from the solid. Oxygen atoms from the solid surface (O_s) are involved in this reaction (Equations 2 and 3):

$^{18}O_2 + {}^{16}O_s \rightarrow {}^{16}O{}^{18}O + {}^{18}O_s$ (2)

$^{16}O{}^{18}O + {}^{16}O_s \rightarrow {}^{16}O_2 + {}^{18}O_s$ (3)

(iii) 2-atoms heterolytic exchange (named r_2) between the gas O_2 molecule and the oxygen atoms from the solid (Equations 4-6):

$^{18}O_2 + 2{}^{16}O_s \rightarrow {}^{16}O_2 + 2{}^{18}O_s$ (4)

$^{16}O{}^{18}O + 2{}^{16}O_s \rightarrow {}^{16}O_2 + {}^{16}O_s + {}^{18}O_s$ (5)

$^{16}O{}^{18}O + 2{}^{18}O_s \rightarrow {}^{18}O_2 + {}^{16}O_s + {}^{18}O_s$ (6)

A model derived from Klier *et al.* was used to describe the main processes [24]: both exchange rate and bulk isotope diffusion were involved. Sample particles were modelled as one dimension spherical particles of radius L (m) (90 nm, 112 nm and 1 µm for LSM, LSCF and LNO respectively). The oxygen amount in the sample (N_{ox} atoms) was defined as the sum of oxygen atomic amount in the solid except the surface (N_v atoms) and those located at the surface (N_s atoms). It was determined using crystallographic considerations: 1.3101×10^{-2}, 1.3017×10^{-2} and 1.0125×10^{-2} mol.g^{-1} for LSM, LSCF and LNO respectively. The homomolecular exchange reaction in the gas phase (r_0 constant rate in s^{-1}) was considered as negligible due to the low temperature used for the isothermal isotopic exchange experiments.

In the gas phase, the variation of the ^{18}O fraction α_g was related to the adsorbed amount of oxygen on the oxide following Equation 7:

$$\frac{\partial \alpha_g}{\partial t} = b \cdot r_H \cdot (\alpha_s - \alpha_g) \quad (7)$$

where b is the ratio of the number of oxygen atoms at the surface N_s of the solid compared to the gas phase N_g, r_H the rate constant for the heteroexchange reactions ($r_H = 0.5r_1 + r_2$ in s^{-1}) and α_s the ^{18}O fraction at the oxide surface.

At the gas/solid interface, the oxygen atoms were assumed to be identical to the bulk (homogeneous surface) and the number of adsorbed oxygen was considered negligible compared to the number of oxygen atoms in the oxide surface. The variation of the atomic fraction of ^{18}O at the surface of the sphere α_s was given by the quantity adsorbed on this surface from which was subtracted the quantity which diffuses in the solid (Equation 8):

$$\frac{\partial \alpha_s}{\partial t} = r_H \cdot (\alpha_g - \alpha_s) - 3 \cdot b_s \cdot \frac{D}{L} \cdot \frac{\partial \alpha}{\partial R}\Big|_{R=L} \quad (8)$$

where b_s is ratio between N_v which is the oxygen atomic amount in the solid except the surface and N_s the oxygen atomic amount at the surface. D (m^2 s^{-1}) is the effective diffusion coefficient inside the particle.

In the solid, the second Fick's law was considered for the diffusion according to Equation 9:

$$\frac{\partial \alpha}{\partial t} = \frac{D}{R^2} \cdot \frac{\partial}{\partial R} \cdot \left(R^2 \frac{\partial \alpha}{\partial R}\right) \quad (9)$$

where α is the ^{18}O fraction in the solid except the surface, D the already defined diffusion coefficient and R the coordinate along the oxide particle radius (m).

The variation of the $^{16}O{}^{18}O$ gas fraction x_{34} is given by Equation 10:

$$\frac{\partial x_{34}}{\partial t} = b\{r_0[2\alpha_g(1-\alpha_g) - x_{34}] + r_1[\alpha_g(1-\alpha_s) + \alpha_s(1-\alpha_g) - x_{34}] + r_2[2\alpha_s(1-\alpha_s-x_{34})]\} \quad (10)$$

Using the definition of the ^{18}O fraction α_g (Equation 11):

$$\alpha_g = \frac{1}{2}x_{34} + x_{36} \quad (11)$$

and the sum of all oxygen atomic fractions (Equation 12):

$$x_{32} + x_{34} + x_{36} = 1 \quad (12)$$

the calculated $^{16}O_2$ and $^{18}O_2$ gas fraction could be determined as a function of ^{18}O fraction α_g and the $^{16}O^{18}O$ gas fraction x_{34} with the following Equations 13 and 14:

$$x_{32} = 1 - \alpha_g - \frac{x_{34}}{2} \quad (13)$$

$$x_{36} = \alpha_g - \frac{x_{34}}{2} \quad (14)$$

The initial conditions were set as a known amount of ^{18}O oxygen in the gas phase and none at the surface nor in the oxide (the natural abundance of ^{18}O in oxide was neglected). The boundary conditions were expressed by a finite concentration at the core of the oxide particle (Equation 15):

$$\left.\frac{\partial \alpha}{\partial R}\right|_{R=0} = 0 \quad (15)$$

and by an identical atomic fraction at the surface and in the oxide volume (Equation 16):

$$\alpha|_{R=L} = \alpha_s \quad (16)$$

Using an homemade software written in Python, this system of 3 equations (in adimensional forms) was solved by the method of lines (70 points along the characteristic length *L* were used) [26]. The number of points used was adjusted in order to obtain invariance of the results. Fraction profiles ($^{16}O_2$, $^{16}O^{18}O$ and $^{18}O_2$ in the gas phase) as a function of time were obtained with the numerical solution of this system. Then, the physicochemical parameters were determined from the experimental gas fraction curves using the global particle swarm optimization method (PSO) [27]. This method is a very popular optimization which has been successfully applied to the kinetic parameters estimation problem [28]. The following parameters were applied: 20 swarm particles over 1000 iterations and $1x10^{-8}$ as minimal change in the swarm's best objective value. The sum of squared residuals was used as the minimizing function (Equation 17):

$$\sigma = \sum_{i=1}^{n}\left(x_{32}^{exp} - x_{32}^{calc}\right)^2 + \sum_{i=1}^{n}\left(x_{34}^{exp} - x_{34}^{calc}\right)^2 + \sum_{i=1}^{n}\left(x_{36}^{exp} - x_{36}^{calc}\right)^2 \quad (17)$$

where x_{32}, x_{34} and x_{36} are mole fractions of oxygen molecules of three different isotopic compositions $^{16}O_2$, $^{16}O^{18}O$ and $^{18}O_2$ in the gas phase, indexes *exp* and *calc* are related to experimental and calculated values of oxygen mole fractions. Figure 1 shows the temperature programmed oxygen isotopic exchange (TPOIE) over LSM, LSCF and LNO. Commercial powders of LSM and LSCF were used, whereas LNO was synthetized by solid-state reaction. The powder X-ray diffraction of the synthesised LNO is plotted in Figure S1. Single phase was obtained without detecting any secondary phase. [17] Two regimes are observed in the case of LSM. The first at low temperature (ca. 360°C) and the second one at higher temperature (ca. 500°C). This behaviour is similar to the one observed for $LaMnO_3$. [29] Those two regimes are attributed to surface and subsurface diffusion at low temperature, whereas bulk diffusion is triggered at higher temperature. Oxygen exchange on LSCF starts at low temperature (ca. 250°C) and quickly reaches its equilibrium value at 420°C indicating that all oxygen atoms from the gas phase are easily exchangeable with oxygen atoms from the oxide. For LNO, oxygen exchange begins at 360°C and reaches equilibrium at 500°C.

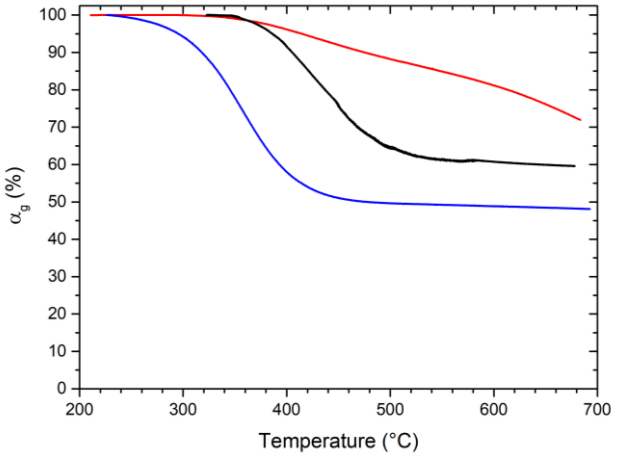

Figure 1. Temperature programmed oxygen isotopic exchange on powder samples of LSM with 53 mbar $^{18}O_2$ (red), LSCF with 53 mbar $^{18}O_2$ (blue) and LNO with 79 mbar $^{18}O_2$ (black). $^{18}O_2$ pressures were chosen to keep a constant $^{18}O_{(g)}/^{16}O_{(s)}$ ratio for all measurement. Temperature ramp = 5°C.min^{-1}.

Fitting of α_g with the model at different temperatures (Figure 2) allows determining r_1, r_2, r_H and their corresponding activation energies, the results are shown in Table 1. In the case of LSM the one atom heteroexchange is the dominant mechanism for oxygen exchange at all investigated temperatures as shown by the value of the relative proportion X_1. In the case of LSCF, the one atom heteroexchange mechanism is favoured at low temperature and tends to decrease in favour of the two atoms heteroexchange (the X_2 value increases with temperature). This corresponds to the temperature where the O^{2-} ionic conductivity becomes appreciable. Therefore, we can attribute the one atom heteroexchange to the electronic properties whereas the two atoms heteroexchange is mostly due to the ionic conductivity of the oxide. LNO, which is also a MIEC, behaves differently from LSCF since only the 2 atoms heteroexchange is identified over the temperature range. The overall heteroexchange properties are reflected by r_H (determined from Equation 7). Activation energies for r_H are 76 kJ.mol^{-1}, 74 kJ.mol^{-1} and 17 kJ.mol^{-1} for LSM, LSCF and LNO respectively. These activation energies for heteroexchange are quite different from literature values. For LSM, the activation energy for the surface exchange coefficient k* is 128 kJ.mol^{-1} when determined from Isotope exchange / depth profile on a dense sample. [11] For LSCF, a value of 45.4 kJ.mol^{-1} below 500°C was obtained from isothermal isotope exchange on powder sample. [30] Concerning LNO, apparent activation energies for surface exchange are generally ranging from 120 to 140 kJ.mol^{-1}, although much smaller values were reported. [22b]

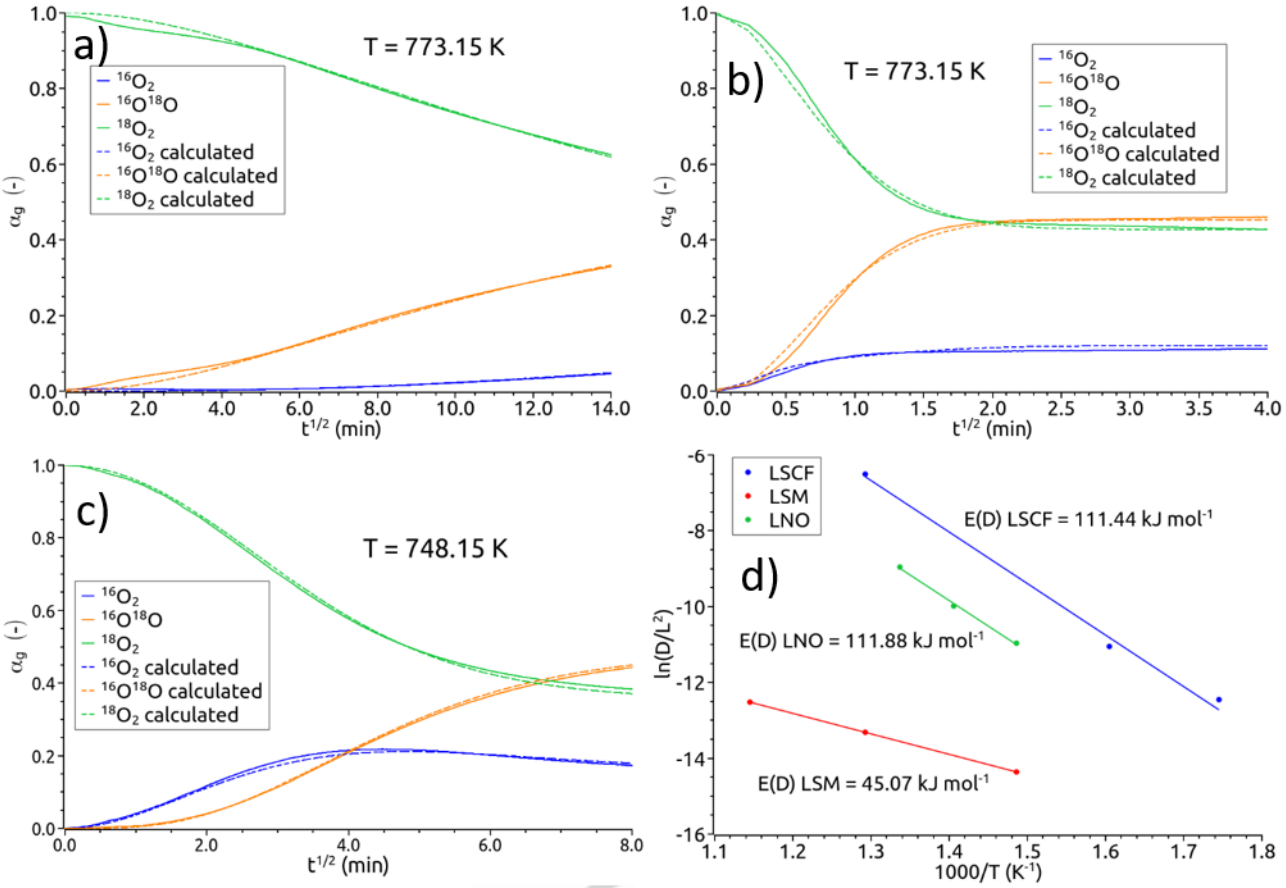

Figure 2. Isothermal OIE for a) LSM at 500°C, b) LSCF at 500°C, c) LNO at 475°C and d) Arrhenius plot of the bulk oxygen diffusion coefficient.

It is difficult to explain these discrepancies, although it is known that the sample morphology (powder, dense sample, porous electrodes (where the gas diffusion can affect the mass transport) as well as the employed method (Electrical conductivity relaxation (ECR), oxygen isotopic exchange (OIE), electrochemical impedance spectroscopy (EIS)) can give quite different results. [31]

Electrochemical Characterizations of Symmetrical Cells

Symmetrical cells were prepared by screen printing inks of LSM, LSCF and LNO on dense 8-YSZ substrates 248 µm thick (see experimental section). Interfacial layers of ceria doped gadolinium oxide (CGO) were employed for the LSM and LSCF cells to inhibit the reactivity between the catalysts and YSZ electrolyte. As preliminary tests, no CGO layer was employed for LNO symmetrical cells. The porous electrode layers obtained is typically 23 µm thick as measured by X-ray tomography (Figure 3) on the LSM symmetrical cell. The CGO interfacial layer (average of 9 µm thickness) is not totally flat nor smooth and the agglomerated particles present some voids in the dense YSZ coverage (Figure S2). Consequently, one cannot exclude the possibility of some remaining LSM/YSZ and LSCF/YSZ direct interface. Figure 4 shows the electrochemical impedance spectra, linear scan voltammetries and corresponding Tafel plots obtained for the three symmetrical cells at 600°C. Nyquist plots measured at open circuit voltage (OCV) at 600°C are shown for LSM (Figure 4a), LSCF (Figure 4d) and LNO (Figure 4g) symmetrical cells. Typical spectrum of porous LSM is obtained at 600°C with a large low frequency arc related to gas diffusion in the porous structure (mass transfer resistance) particularly pronounced at 20 mbar O_2 and a high frequency arc attributed to electrode kinetics. [5] The LSCF electrode displays also the expected electrochemical behaviour with mostly three visible contributions at OCV. The high frequency contribution is attributed to the LSCF/CGO interphase charge transfer, the mid frequency to oxygen surface exchange and the low frequency contribution to gas phase O_2 diffusion in pores. [32] The LNO electrode is characterized by two depressed semi circles. Its ohmic resistance is higher than that of LSM and LSCF cells at the same temperature, LNO being known to react with the YSZ electrolyte material forming insulating $La_2Zr_2O_7$ or $SrZrO_3$ particles at the electrode/electrolyte interphase when sintered at high temperature. [17] Two processes are observed at medium and low frequency with a higher impedance for the process at mid frequency, as reported in the literature at low P_{O2} [22c]. The contribution at mid frequency (kHz) is associated to interfacial ionic transfer impedance between the electrode material and the YSZ electrolyte, and the low frequency contribution (Hz) to the electrode reaction process (molecular oxygen dissociation and adsorption phenomena). [17, 22c]

Table 1. Physicochemical parameters obtained from the refinement of oxygen gas fraction curves using global particle swarm optimization method. Heteroexchange rate constants (r_1, r_2 and r_H) and diffusion coefficient related to the characteristic length (D/L^2) are given with the coefficient of determination (R^2). Relative proportions of r_1 (X_1) and r_2 (X_2) for the whole exchange process are calculated. Assuming an Arrhenius law within the temperature range explored for each material, values for activation energy are also tabulated.

	LSM			LSCF			LNO		
T (K)	673	773	873	573	623	773	673	711	748
r_1 (× 10^{-3} s^{-1})	1.58	10.05	41.80	1.09	7.26	51.67	- [a]	- [a]	- [a]
X_1 (-) [b]	0.9095	0.9770	0.9921	0.7959	0.6901	0.6278	- [a]	- [a]	- [a]
E_a (r_1) (kJ.mol^{-1})	79.97			68.02			- [a]		
r_2 (× 10^{-3} s^{-1})	0.16	0.24	0.33	0.28	3.26	30.63	1.54	1.85	2.07
X_2 (-) [b]	0.0905	0.0230	0.0079	0.2041	0.3099	0.3722	1.0000	1.0000	1.0000
E_a (r_2) (kJ.mol^{-1})	18.28			82.12			16.65		
r_H (× 10^{-3} s^{-1})	0.95	5.26	21.23	0.82	6.89	56.47	1.54	1.85	2.07
E_a (r_H) (kJ.mol^{-1})	75.83			74.30			16.65		
D/L^2 (× 10^{-5} s^{-1})	0.058	0.163	0.368	0.39	1.59	148.73	1.73	4.58	12.89
E_a (D) (kJ.mol^{-1})	45.07			111.44			111.88		
R^2	0.9998	0.9998	0.9962	0.9992	0.9998	0.9989	0.9960	0.9940	0.9979

[a] The calculated values are negligible (< 1×10^{-16} s^{-1}). [b] The relative proportion X_i is defined as $X_i = r_1 / (r_1 + r_2)$.

Despite the possible formation of $La_2Zr_2O_7$ or $SrZrO_3$ at the LNO/YSZ interphase (which can partially hinder the O^{2-} ionic diffusion from LNO to YSZ), no additional processes were observed on the EIS spectra at 600°C (Figure 4g) nor at 700°C (Figure S3) so the cell was used for further experimentations. Polarization curves (without and with ohmic drop correction) are shown on Figure 4b, 4e and 4h for LSM, LSCF and LNO respectively. The current density evolution for LSM cell (Figure 4b) and LNO cell (Figure 4h) at low cell voltage (-0.4 V < ΔE < 0.4 V) is rather flat. In this domain, the main process involved is O_2 reacting directly from the gas phase to the TPB, as the number of these actives sites is rather limited compared to the whole porous electrode surface. Then, the current density increases exponentially which indicates that the electrochemical process involves the surface diffusion path in addition to the gas/TPB path. It is worth noting that the current density is rather small on LNO, possibly due to zirconate formation at the LNO/YSZ interphase. The LSCF electrode (Figure 4e) shows rapid electrochemical kinetics with the highest current densities among the three electrodes investigated. Corresponding Tafel plots are shown in Figures 4c, 4f and 4i at 600°C for LSM, LSCF and LNO respectively where log I is plotted as a function of electrode overpotential (η). Since no reference electrode is used in the experimental setup, one must estimate the overpotential magnitude. As the polarization curves are reasonably symmetrical (Figures 4b, 4e and 4h), we can consider that the total driving force ($\Delta E = \eta_{anode} - \eta_{cathode}$) is equally split in two parts, half for the oxygen evolution reaction (OER) at the anode and half for the ORR at the cathode. In other words, we consider by this hypothesis that α symmetry coefficient (in the sense of Marcus Hush) is equal to 0.5, which is not rigorously exact as experimentally demonstrated by Monaco *et al.* on LSCF symmetrical cells. [33] To evaluate this hypothesis, we performed polarization curves at 700°C on a LNO symmetrical cell including a platinum reference electrode (Figure S4).

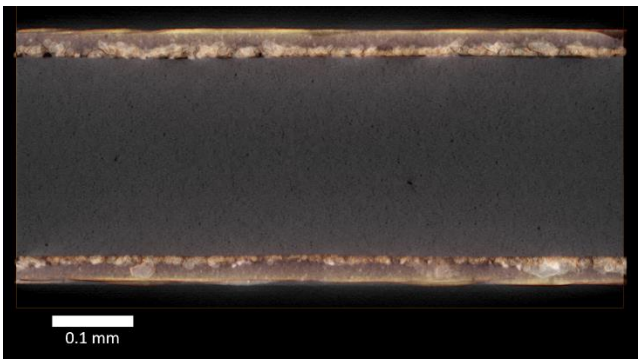

Figure 3. X-ray tomography realized on the LSM symmetrical cell.

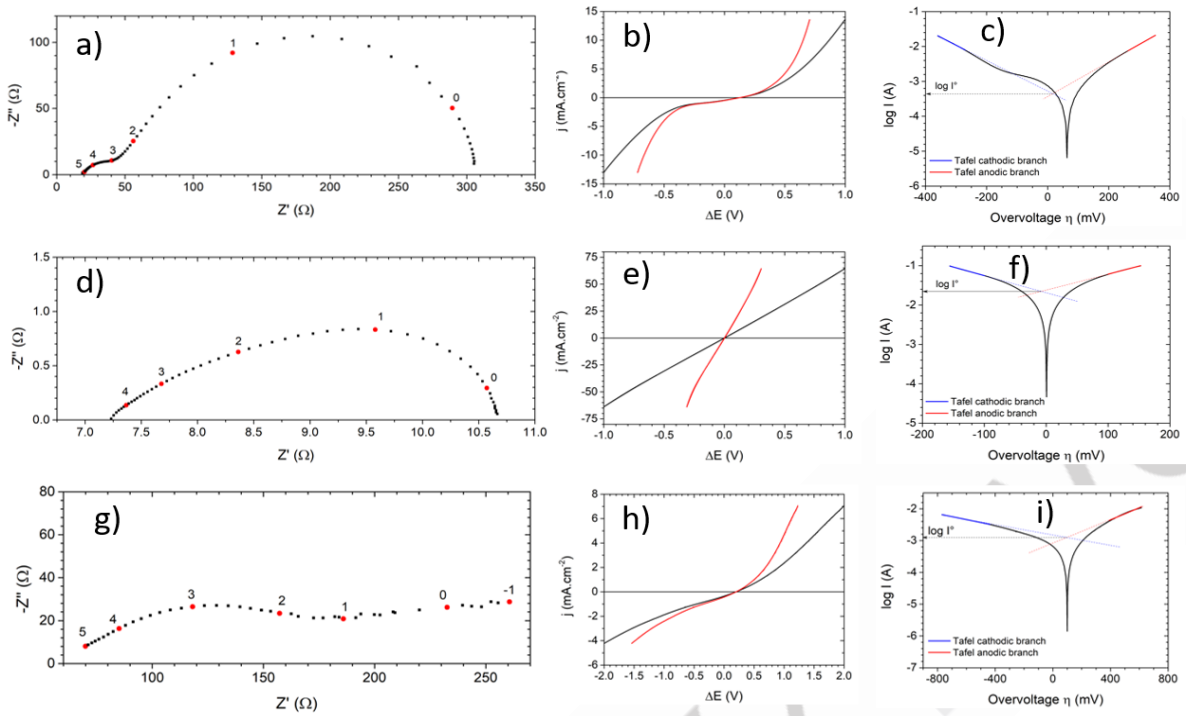

Figure 4. Electrochemical characterizations performed on symmetrical cells at 600°C: Nyquist plots at open circuit voltage (OCV) for a) LSM with 20 mbar O_2, d) LSCF with 15 mbar O_2, and g) LNO with 50 mbar O_2. Red circles indicate decades of frequency. Linear scan voltammetries (20 mV.s^{-1}) measured on symmetrical cells at 600°C for b) LSM with 20 mbar O_2, e) LSCF with 15 mbar O_2, and h) LNO with 50 mbar O_2. Black curves correspond to raw measurement, red curves are ohmic drop corrected voltammetries. Corresponding Tafel plots for c) LSM, f) LSCF and i) LNO.

It seems that this hypothesis is reasonable for estimating the anodic overvoltage, but leads to an underestimation of the cathodic overvoltage. In this way, the overvoltage η at one electrode can be calculated with Equation 18:

$$\eta = \frac{\Delta E - R_{HF} I}{2} \qquad (18)$$

Where η is the overvoltage (V), ΔE is the applied cell voltage (V), R_{HF} is the sum of all ohmic resistances (electrolyte ionic conductivity, electrical contacts, cables) determined as the high frequency intercept with the real axis in the Nyquist diagram (Ω) and I the current (A). The term $\Delta E - R_{HF} I$ corresponds to the ohmic drop correction (in Figure 4b, 4e and 4h). Exchange current densities (j°) are determined from the intersection of Tafel cathodic and anodic branches at an overvoltage close to η = 0 V. The exchange current density is proportional to the surface exchange coefficient k* according to Equation 19: [14]

$$j° = \frac{4Fk^*[O^{2-}]}{A} \qquad (19)$$

Where j° is the exchange current density (A.cm^{-2}), F is the Faraday constant (C.mol^{-1}), k* is the surface exchange coefficient (cm.s^{-1}), [O^{2-}] is the bulk concentration of oxide ions in the oxide electrode (mol.cm^{-3}) and A is electrode area (cm²). Therefore, comparing j° values is a convenient way to evaluate the evolution of k*. Table 2 shows the values of j° for the three electrodes at different temperatures as well as corresponding activation energies. For LSCF, the obtained values of j° are very well matching with those obtained by Esquirol et al. [14] As expected from the polarization curves, j° is much higher in the case of LSCF than LNO and LSM. Apparent activation energies were estimated from j° values for the three electrode materials investigated. These are quite different from those obtained from OIE experiments on powders for r_H (Table 1), indicating that hetero-exchange activation energy (r_H) (or to the surface exchange coefficient k*) is sensitive to the material morphology (powder *vs.* porous electrode).

Table 2. Exchange current densities (j° / mA.cm^{-2}) extracted from Tafel plots and corresponding activation energy (E_a / kJ.mol^{-1}).

Temperature (°C)	LSM	LSCF	LNO
400	0.0135	0.0464	n.d.
500	0.0560	0.748	n.d.
600	0.253	14.05	0.712
700	n.d.	n.d.	3.978
E_a(j°) kJ.mol^{-1}	71	139	122

Polarized Oxygen Isotopic Exchange (POIE) on Symmetrical Cells

Figure 5 shows typical POIE experiments along with the fitting of α_g *vs.* time. One can distinguish two different behaviours: i) a dominant one oxygen atom heteroexchange mechanism in the case of LSM and LNO (Figures 5a and 5e respectively). This is exemplified by the majority formation of the $^{16}O^{18}O$ isotopologue (m/z = 34) (Equation 2) and ii) a dominant two oxygen atoms heteroexchange mechanism in the case of LSCF (Equation 4) confirmed by the majority formation of $^{16}O_2$ isotopologue (m/z = 32). This observation is in agreement with the dominant mechanism observed on LSM and LSCF powders, where at high temperature the one atom heteroexchange is the main mechanism observed for LSM whereas the two atoms heteroexchange is the main mechanism observed for LSCF (Table 1). However, LNO displays a dominant one atom heteroexchange on the POIE experiments (Figure 5e) whereas the two atoms heteroexchange is the main mechanism on powder OIE (Figure 2c). The two atoms heteroexchange mechanism is most probably related to the MIEC properties of the catalyst, where two adsorbed ^{18}O atoms coming from the dissociative adsorption of $^{18}O_2$ can be more easily incorporated in the bulk of the MIEC (the bulk path) than diffusing to the TPB and then incorporating in the YSZ electrolyte. The latter mechanism (TPB way or surface path) is more likely to proceed via a one atom heteroexchange. This discrepancy between powder LNO and LNO symmetrical cell can arise from the formation of the insulating pyrochlore or zirconate layer at the electrode/electrolyte interphase which in turn blocks the O^{2-} incorporation into YSZ, thus favouring the TPB pathway. In all POIE experiments, the electrical current is quite stable with time indicating that electrodes reach steady state during the polarized isotopic exchange experiments. The ^{18}O gas atomic fraction (α_g) is determined from Equation 11 and its evolution with time is plotted on Figures 5b, 5d and 5f for LSM, LSCF and LNO respectively. Kinetics of oxygen exchange are assumed to be first or pseudo-first order reactions, implying that molecular oxygen is involved in the rate determining step (rds). [34] Two distinct kinetic models are proposed. In the case of LSM and LNO (where the one atom heteroexchange prevails), a simple first order decay of α_g as a function of time is observed and can be described with Equation 20:

$$a_g = A\, exp^{-kt} \qquad (20)$$

where A is the pre-exponential factor (same unit as α_g and is close to 100 %), k is the first order rate constant of the rds (s^{-1}) and t is time (s). The rate constant describes the surface path. In the situation of LSCF (where the two atoms heteroexchange prevails), the simple first order decay shown in Equation 20 does not fit correctly the data (Figure 5d) where it seems that two kinetic constants are observed. The kinetic model used for LSCF is therefore involving a competitive two first order reactions (Equation 21):

$$a_g = A_{fast}\, exp^{-k_{fast}t} + A_{slow}\, exp^{-k_{slow}t} \qquad (21)$$

Where the pre-exponential factors A_{fast} and A_{slow} are the weight (or population) of oxygen atoms following the fast and slow pathway respectively (%), k_{fast} and k_{slow} are the corresponding first order rate constants.

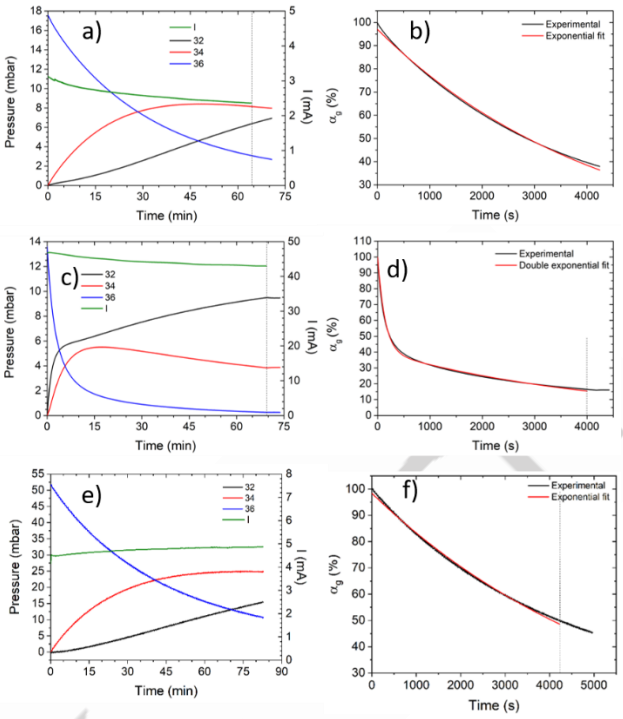

Figure 5. Polarized oxygen isotopic exchange experiments and corresponding kinetic modelling of alpha vs. time. a-b) LSM at 600°C – η = 132 mV, c-d) LSCF at 500°C – η = 343 mV, e-f) LNO at 700°C – η = 147 mV.

This model describes the two different possible paths that can occur on such a MIEC electrode: the surface path and the bulk path. [33] As the two atoms heteroexchange prevails, we therefore assign k_{fast} to the bulk path and k_{slow} to the surface path. By fitting the α_g = f(t) curves obtained for LSM, LSCF and LNO with the appropriate kinetic model, one can evaluate the evolution of first order rate constants as a function of temperature as well as the overvoltage (η). It is worth noting that these kinetic constants are related to surface reactions and are expressed in s^{-1}. Usually, the surface exchange coefficient (k_s^* expressed in $cm.s^{-1}$) is used to characterize the surface exchange properties and is expressed as a first order kinetic constant normalized to a characteristic length (Δx). The $cm.s^{-1}$ unit was not chosen in the present study since the choice of this characteristic length requires the knowledge of the rate determining step, i.e. the distance over which an electron is transferred from substrate to adsorbate in the case of a rds involving an electron transfer, what can be approximated to be the cation-anion distance in the oxide. [10] Obtained kinetic constants as well as pre-exponential factors can be found in Tables S1, S2, and S3 for LSM, LSCF and LNO respectively. Figure 6 shows the evolution of k (surface path, Equation 20) in the case of LSM as a function of temperature and overvoltage. It can be observed that k is increasing with the applied overvoltage, and the magnitude of this increase is higher at high temperature. This behaviour is similar to the one observed for POIE realized on a Pt/YSZ/Pt symmetrical cell, where only the surface path is allowed. [9]

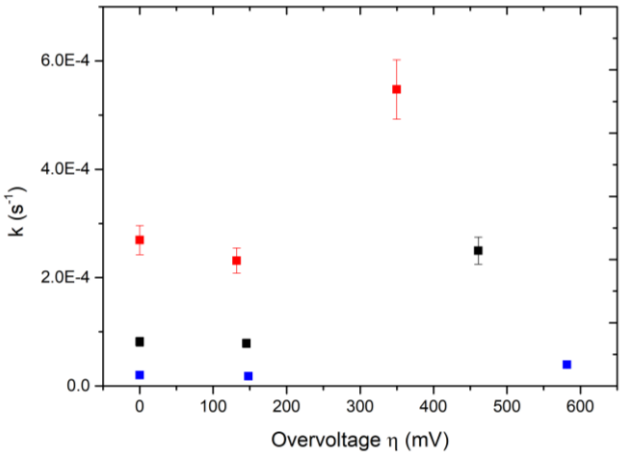

Figure 6. First order kinetic constant k (surface path) as a function of applied overvoltage (η) obtained for LSM during POIE at P_{O2} = 20 mbar at 400°C (blue), 500°C (black) and 600°C (red). Error bars estimated at 10 %.

Equation 20 describes well the experimental data at the exception of the largest overpotential value at 600°C (Table S1). In this situation, oxygen vacancies formation in the bulk of LSM are stimulated by the high overvoltage thus inducing an ionic conductivity.[13] Figure 7a shows the evolution of k_{slow} (surface path) as a function of temperature and overvoltage for LSCF. This evolution is very similar to the one observed for LSM (Figure 6) and for Pt [9] which gives an additional confirmation that the rate constant for the surface path is significantly enhanced by the applied overvoltage. A possible explanation for it can be that the surface exchange coefficient (k*) is positively dependent on η and this increase is more pronounced as the temperature increases, as also suggested by other authors, the magnitude of increase being close to that study. [8, 15] In contrast, k_{fast} (bulk path) is almost independent of η in the temperature range investigated (Figure 7b), although at 600°C a slight increase is observed at high η. Equation 21 used to extract k_{slow} and k_{fast} fits correctly the experimental data although a slight deviation is observed at 600°C (Table S2). As proposed by Laurencin *et al*. [35], "*the relative proportion of surface to bulk paths can be expressed through the ξ indicator defined as the ratio between the kinetic rates of direct oxidation* (or reduction) *at TPB* (the surface path) *and oxygen incorporation / excorporation from LSCF* (the bulk path)". In our situation, we discriminate between the rate constants for surface and bulk path (k_{slow} and k_{fast}) and between the oxygen populations that follow the surface or bulk mechanism (the A_{slow} and A_{fast} pre-exponential factors in Equation 21, Table S2). Doing so, the ratio A_{slow}/A_{fast} must be reflecting the as defined ξ indicator. ξ as a function of overvoltage (η) is plotted in Figure 8 at 400°C, 500°C and 600°C. It can be noticed that at low temperature (400°C), the surface path is favoured (ξ > 1). That is not surprising since the ionic conductivity of LSCF is rather low at this temperature.

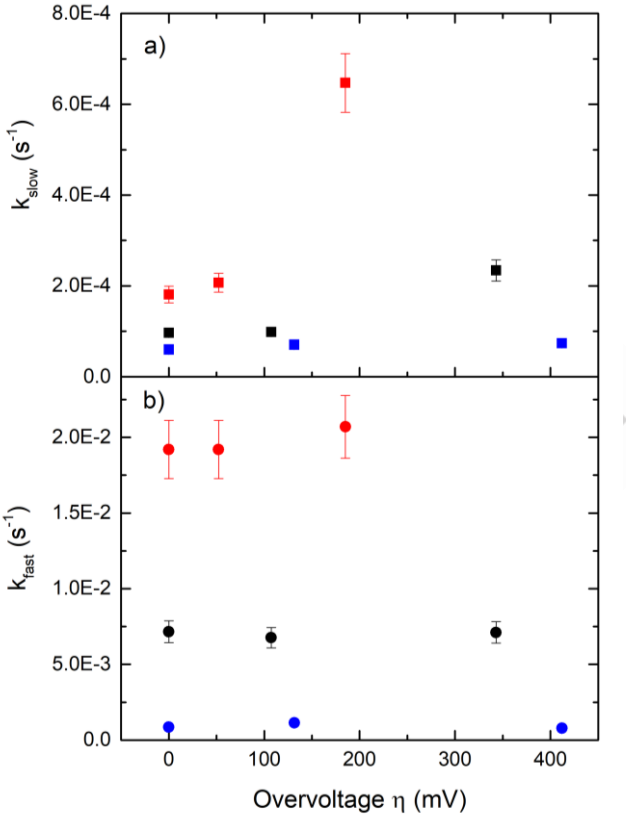

Figure 7. First order kinetic constants as a function of applied overvoltage obtained for LSCF during POIE at P_{O2} = 15 mbar at 400°C, (blue), 500°C (black) and 600°C (red), a) k_{slow} (surface path), b) k_{fast} (bulk path). Error bars estimated at 10 %.

When the temperature comes around the critical temperature where the ionic conductivity is triggered (in this case around 500°C), ξ is close to 1 (i.e. the surface and bulk paths are balancing). Above this critical temperature (500°C), the bulk path is favoured (ξ < 1). It is interesting to note that at all investigated temperatures, ξ is decreasing with overvoltage (η), thus η is favouring the bulk path in terms of oxygen population (and not on the basis of rate constants), whereas an increase in η favours the kinetic constant for surface exchange (Figures 6, 7a and [9]). This surprising result is probably resulting from the two orders of magnitude between k_{fast} and k_{slow} (Figures 7a and 7b). It is important to point out that these results were obtained at low oxygen partial pressure (P_{O2} = 15 mbar), which favours the formation of oxygen vacancies in the bulk of LSCF. Our observations are in contradiction with the work of Monaco *et al.* [33] In their study, they evidenced a transition from bulk to surface path when an anodic polarization is applied at temperatures between 700 and 800°C at P_{O2} = 210 mbar.

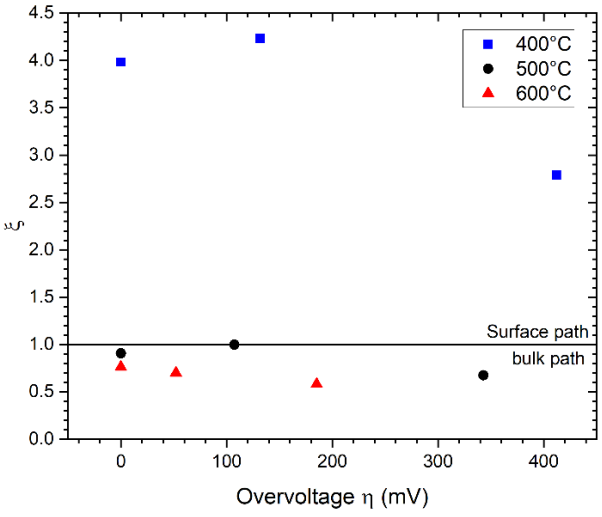

Figure 8. Plot of the surface to bulk ratio (ξ) as a function of the overvoltage (η) at 400°C (blue), 500°C (black) and 600°C (red) for LSCF (P_{O2} = 15 mbar).

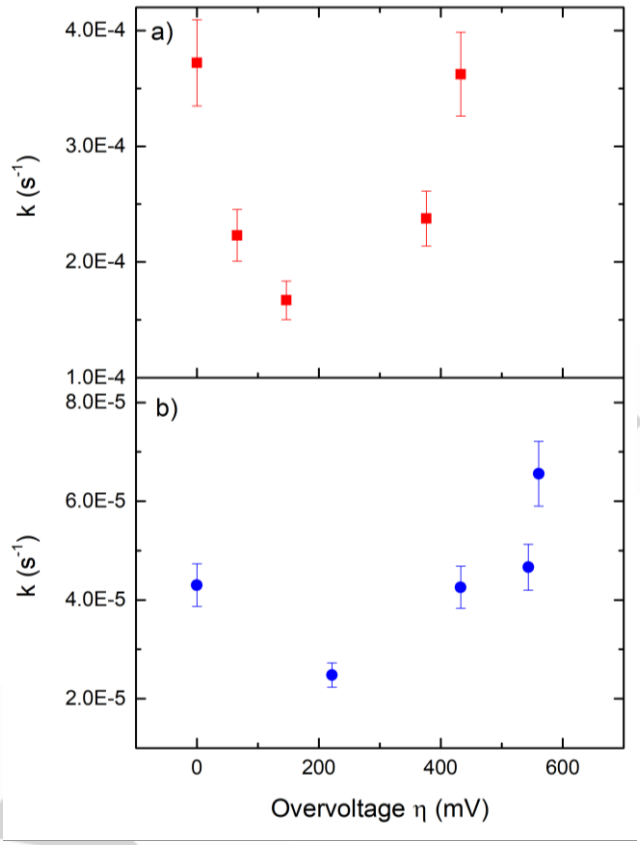

Figure 9. Kinetic constant k (surface path) as a function of applied overvoltage obtained for LNO during POIE at P_{O2} = 50 mbar at a) 700°C and b) 600°C. Error bars were estimated at 10 % based on the variation of the cell polarization resistance (R_p) measured at OCV prior each experiment (Figure S3).

They used a three-electrode configuration that allows the observation of one electrode independently in the OER configuration (anodic polarization) whereas we used a two-electrode configuration and we estimate the electrode overvoltage by assuming that OER and ORR are symmetrical processes (Equation 18), while the overall process OER + ORR is investigated. This might explain these discrepancies. In the case of LNO, where the surface path is dominant (possibly due the formation of an insulating layer at the LNO/YSZ interphase which partially blocks the O^{2-} transfer from bulk LNO to YSZ), a surprising inverted bell like evolution of k (surface path) with η is observed, showing an initial decrease to reach a minimum and then a significant increase at high η as expected for the surface path (Figure 9). This trend is observed both at 700°C and 600°C (the experiment was further confirmed with another symmetrical cell at 700°C, Figure S5). The initial inhibition of k at small overpotential (η < 200 mV) may be explained by a significant modification of the surface properties of LNO cathode (ORR) induced by a decrease of the oxygen overstoichiometry with overvoltage compared to the measure at the OCV. Since the overstoichiometry (+δ) is responsible for the ionic conduction properties as well as electronic conduction properties a decrease of the overstoichiometry would lower k; it can be that the cathode (ORR) exhibits a lower value of δ compared to the anode (OER) at low overpotential as shown in Figure S4). Further investigations are necessary to clarify this behavior. Scheme 1 resumes the different pathways for oxygen incorporation in the electrolyte, namely the surface and bulk paths. Globally, it was demonstrated that the rate constant of the surface path is significantly enhanced by increasing the overpotential, which might indicate that the surface exchange coefficient is increased with the overpotential. Contrarily, the rate constant for the bulk path seems to be independent of η. The rate constant for the surface path is ca. two orders of magnitude lower than the one for the bulk path. Therefore, the balance surface/bulk is drove by the temperature as well as the applied overvoltage.

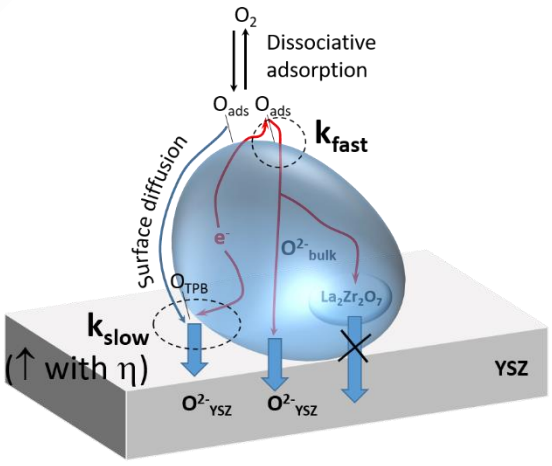

Scheme 1. Representation of the surface and bulk mechanisms for oxygen exchange.

Conclusion

Three state of the art materials used in Solid Oxide Electrolyser Cells were investigated in terms of oxygen activation, surface and bulk diffusion. Oxygen Isotopic Exchange on powders was modelled in a way that heteroexchange reactions are split between a one or two atoms reactions. The one atom heteroexchange mechanism is attributed to the electronic properties of the oxide and to the surface diffusion, whereas the two atoms heteroexchange mechanism is attributed to the ionic conductivity of the oxide and to the bulk diffusion. Polarized Oxygen Isotopic Exchange on symmetrical cells was employed to evaluate the influence of electrode overpotential on the surface and bulk pathways. It is demonstrated that the surface path is greatly enhanced by increasing the overpotential, where its influence on the bulk path seems to be negligible. These findings provides mechanistic information on the different pathways for oxygen mobility in a SOEC and gives insights for orientating this mobility through the surface or bulk paths. This orientation can be realized by tuning the balance between electrical and ionic conductivity. Moreover, the applied overvoltage is an additional parameter that can be used for orientate oxygen mobility in the electrode material. This may provide insights for the choice of an adequate electrode material in SOEC systems involving coupled catalytic oxidation reactions such as natural gas assisted CO_2 + H_2O co-electrolysis to generate valuable CH_4 oxidation products such as ethylene or syngas.

Experimental section

Electrode catalysts

$La_2NiO_{4+\delta}$ was synthesized by solid-state reaction. Prior to weighting, La_2O_3 (Sigma-aldrich 99.9%) was dried at 1000°C and NiO (Thermofisher scientific, 99%) was dried at 300°C for two hours. The oxides were mixed with acetone in an agate mortar, pressed with a uniaxial press and sintered at 1050°C for 10h in air. The resulting pellet was ground with an agate mortar into powder, pressed and sintered at 1200°C for 10h in air. The pellet was ground into a powder for further characterization. The powder X-ray diffraction was done with a Bruker D8 advance Davinci 2 with Cu $K_{\alpha1}$ = 1.5406 Å and Cu $K_{\alpha2}$ = 1.5439 Å, 2θ from 10° to 100° with a step of 0.03° and 1.5s per step.

Oxygen isotopic exchange on powders

Isotopic oxygen exchange experiments were carried out in a closed recycling reactor system. A recirculating pump was used in order to avoid any diffusion and mass transport effects in the gas phase that affect partial pressures of different isotopologues measured by mass spectrometry (Pfeiffer Vacuum). The used reactor system is described in more detail in [36]. Temperature-programmed oxygen isotopic exchange (TPOIE) were carried out on 20.0 mg of LSCF, 19.9 mg of LSM and 25.4 mg of LNO. Samples were then activated with pure $^{16}O_2$ at 700°C for 1 h before being cooled down for TPOIE. This activation step released the material surface from adsorbed species such as carbonates that could influence oxygen exchange activity. The system was then purged (using vacuum) and the $^{18}O_2$ molecule charged (53 mbar for LSCF and LSM and 79 mbar for LNO; 99.9% purity, supplied by Isotec). For each experiment, the ratio between the introduced amount of ^{18}O atoms in the gas phase and the number of ^{16}O contained in the sample, is kept constant. In the case of LNO the increased amount $^{18}O_2$ introduced (necessary to prevent air entering the system) is compensated by a larger sample mass. The ramp rate of the temperature was 5°C / min. The masses 32, 34, 36 m/z were monitored as a function of time to follow the exchange. The m/z values of 18, 28, 44, 46 and 48 were also recorded to follow the possible presence of $H_2{}^{16}O$, $C^{16}O_2$, $C^{16}O^{18}O$, $C^{18}O_2$ molecules in the gas phase.

Symmetrical cells screen printing

GDC powder (Fuellcellmaterials) was screen printed on YSZ button cell (fuel cell material) on both sides and heat treated at 1300°C to obtain GDC/YSZ/GDC button cell. LSM/GDC/YSZ/GDC/LSM and LSCF/GDC/YSZ/GDC/LSCF symmetrical cells were obtained by screen printing LSM powder (Fuellcellmaterials) or LSCF powder (Fuellcellmaterials) followed by a heat treatment at 1100°C.

For the $La_2NiO_{4+\delta}$ / YSZ / $La_2NiO_{4+\delta}$ symmetrical cell preparations and oxygen isotopic exchange on powder, the LNO powder was milled with a high-energy ball mill SPEX sample prep 8000M with YSZ jar and balls. The ink was screen printed on both sides of YSZ substrate (Fuellcellmaterials) and heat treated at 1150°C for two hours in air.

X-ray tomography

X-ray tomographic acquisition of the LSM cell was performed on an EasyTom XL Duo device (RX-solutions, France) with a cooled nanofocus x-ray source equipped with a LaB6 cathode (Hamamatsu L10711) coupled to a flat panel detector (Varian PaxScan 2520DX) and according to the following parameters: 100 kV (tube voltage), 15 µA (target current), 250 nm focal spot size, 1440 projections (1840x1456 pixels; 16 bits), 1 frame per second (imager readout speed), 20 frames averaging, source-to-object and source-to-detector distances of 2.70 mm and 678.38 mm respectively, voxel resolution of 506 nm. Slice reconstructions were done with XAct software (RX-Solutions) with a filtered back projection algorithm, attenuation of beam hardening artefact, corrections of x-ray spot drift and ring artefacts. Image and measurements were performed with Avizo v. 2022.2 (Thermo Fisher Scientific-FEI).

Polarized isotopic exchange

The setup for isotopic exchange under polarisation consists of a coupling of a classic oxygen isotopic exchange setup for powder [36] and a button Cell Test Fixture (ProboStat A normal system, SS/S; NorECs) already described [9]. Pt current collectors were used, connected to a Multi Autolab (Metrohm PGSTAT302N) for electrochemical measurements. Linear scan voltammetries were measured at 20 $mV.s^{-1}$. Electrochemical Impedance Spectra were recorded in the potentiostatic mode with an AC amplitude of 10 mV rms between 10^5 and 10^{-1} Hz. In the case of LNO, ohmic resistance was determined by fitting with the following electrical equivalent circuit: L-R_Ω-(R_1/Q_1)-(R_2-Q_2).

Where L is an inductance, R_Ω, R_1 and R_2, are resistances, and Q_1 and Q_2 are constant phase elements. Gas phase analyses were done with a mass spectrometer (Pfeiffer Vacuum QMS 200 Prisma) with a pressure in the ionization chamber kept at 10^{-6} mbar. The symmetrical cell chambers were vacuumed for 10 minutes before the introduction of ^{18}O. Between each isotopic exchange a flow of pure $^{16}O2$ passed through the symmetrical cell chambers until the amount of ^{18}O detected by the mass spectrometer was negligible. A pressure of 20 mbar was used for LSM and LSCF, for LNO a higher pressure of 50 mbar was used to prevent air entering the system.

Supporting Information

The supporting information includes XRD of LNO, X-ray tomography of the LSM cell, EIS of LNO cell at 700°C, polarization curves of a LNO cell comprising a reference electrode, polarized isotopic exchange performed on another LSM cell, and tables for the calculation of kinetic constants during POIE for LSM, LSCF and LNO.

Acknowledgements

The authors acknowledge financial support from the European Union (ERDF), Région Nouvelle Aquitaine (Project CASTOR), ANR (project CHEEC ANR-20-CE05-0023). This work pertains to the French government program "France2030" (EUR INTREE, reference ANR-18-EURE-0010).

Keywords: Polarized Oxygen Isotopic Exchange • SOEC • Oxygen mobility • MIEC • Oxygen catalysis

[1] a) S. D. Ebbesen, S. H. Jensen, A. Hauch, M. B. Mogensen, *Chem. Rev. (Washington, DC, U. S.)* **2014**, *114*, 10697-10734; b) A. Hauch, R. Küngas, P. Blennow, A. B. Hansen, J. B. Hansen, B. V. Mathiesen, M. B. Mogensen, *Science* **2020**, *370*, 186-193.

[2] Y. Zheng, J. Wang, B. Yu, W. Zhang, J. Chen, J. Qiao, J. Zhang, *Chem. Soc. Rev.* **2017**, *46*, 1427-1463.

[3] a) C. Zhu, S. Hou, X. Hu, J. Lu, F. Chen, K. Xie, *Nature Communications* **2019**, *10*, 1173; b) L. Ye, Z. Shang, K. Xie, *Angew. Chem. Int. Ed.* **2022**, *61*, e202207211; c) A. Caravaca, A. de Lucas-Consuegra, V. J. Ferreira, J. L. Figueiredo, J. L. Faria, J. L. Valverde, F. Dorado, *Appl. Catal. B: Environ.* **2013**, *142-143*, 298-306.

[4] J. Martinez-Frias, A.-Q. Pham, S. M. Aceves, *Int. J. Hydrogen Energy* **2003**, *28*, 483-490.

[5] S. B. Adler, *Chem. Rev. (Washington, DC, U. S.)* **2004**, *104*, 4791-4844.

[6] a) M. A. Morales-Zapata, A. Larrea, M. A. Laguna-Bercero, *Electrochim. Acta* **2023**, *444*, 141970; b) P. Ding, W. Li, H. Zhao, C. Wu, L. Zhao, B. Dong, S. Wang, *Journal of Physics: Materials* **2021**, *4*, 022002.

[7] V. A. Sobyanin, V. I. Sobolev, V. D. Belyaev, A. K. Demin, O. A. Marina, *React. Kinet. Catal. Lett.* **1992**, *47*, 327-332.

[8] E. M. Hopper, E. Perret, B. J. Ingram, H. You, K.-C. Chang, P. M. Baldo, P. H. Fuoss, J. A. Eastman, *J. Phys. Chem. C* **2015**, *119*, 19915-19921.

[9] A. Nau, C. Comminges, N. Bion, *ChemPhysChem* **2020**, *21*, 2357-2363.

[10] R. A. De Souza, *J. Mater. Chem. A* **2017**, *5*, 20334-20350.

[11] R. A. De Souza, J. A. Kilner, J. F. Walker, *Mater. Lett.* **2000**, *43*, 43-52.

[12] J. A. Kilner, Y. Ji, M. F. Carolan, *Solid State Ionics* **2005**, *176*, 937-943.

[13] T. Horita, K. Yamaji, N. Sakai, H. Yokokawa, T. Kawada, T. Kato, *Solid State Ionics* **2000**, *127*, 55-65.

[14] A. Esquirol, N. P. Brandon, J. A. Kilner, M. Mogensen, *J. Electrochem. Soc.* **2004**, *151*, A1847-A1855.

[15] G. Cohn, E. D. Wachsman, *J. Electrochem. Soc.* **2017**, *164*, F3035-F3044.

[16] V. V. Vashook, S. P. Tolochko, L. Yushkevich, L. V. Makhnach, I. F. Kononyuk, H. Altenburg, J. Hauck, H. Ullmann, *Solid State Ionics* **1998**, *110*, 245-253.

[17] H. Zhao, F. Mauvy, C. Lalanne, J. M. Bassat, S. Fourcade, J. C. Grenier, *Solid State Ionics* **2008**, *179*, 2000-2005.

[18] A. Chroneos, D. Parfitt, J. A. Kilner, R. W. Grimes, *J. Mater. Chem.* **2010**, *20*, 266-270.

[19] J.-M. Bassat, M. n. Burriel, O. Wahyudi, R. m. Castaing, M. Ceretti, P. Veber, I. Weill, A. Villesuzanne, J.-C. Grenier, W. Paulus, J. A. Kilner, *J. Phys. Chem. C* **2013**, *117*, 26466-26472.

[20] S. Shigenori, K. Shin-ichi, I. Kenji, S. Yasuo, O. Hirofumi, *Bull. Chem. Soc. Jpn.* **1987**, *60*, 1295-1298.

[21] A. L. Shaula, E. N. Naumovich, A. P. Viskup, V. V. Pankov, A. V. Kovalevsky, V. V. Kharton, *Solid State Ionics* **2009**, *180*, 812-816.

[22] a) H. J. M. Bouwmeester, C. Song, J. Zhu, J. Yi, M. van Sint Annaland, B. A. Boukamp, *Phys. Chem. Chem. Phys.* **2009**, *11*, 9640-9643; b) M. V. Ananyev, E. S. Tropin, V. A. Eremin, A. S. Farlenkov, A. S. Smirnov, A. A. Kolchugin, N. M. Porotnikova, A. V. Khodimchuk, A. V. Berenov, E. K. Kurumchin, *Phys. Chem. Chem. Phys.* **2016**, *18*, 9102-9111; c) M. J. Escudero, A. Aguadero, J. A. Alonso, L. Daza, *J. Electroanal. Chem.* **2007**, *611*, 107-116.

[23] V. Vibhu, A. Flura, A. Rougier, C. Nicollet, S. Fourcade, T. Hungria, J.-C. Grenier, J.-M. Bassat, *Journal of Energy Chemistry* **2020**, *46*, 62-70.

[24] K. Klier, J. Nováková, P. Jíru, *J. Catal.* **1963**, *2*, 479-484.

[25] V. S. Muzykantov, V. V. Popovskii, G. R. Boreskov, *Kinet. Katal.* **1964**, *4*, 624-629.

[26] J. Krank, *The mathematics of diffusion*, 2nd ed., Clarendon Press, Oxford, **1975**.

[27] R. Poli, *Journal of Artificial Evolution & Applications* **2008**, 1-10.

[28] A. C. C. Carlos, C. Juan Carlos Fuentes, in *Lecture Notes in Computer Science, Vol. 4827* (Ed.: A. Gelbukh, Kuri Morales, Á.F.), Springer, Berlin Heidelberg, **2007**.

[29] M. Richard, F. Can, S. Gil, A. Giroir-Fendler, D. Duprez, N. Bion, *ChemCatChem* **2016**, *8*, 1921-1928.

[30] Y.-L. Huang, C. Pellegrinelli, E. D. Wachsman, *Angew. Chem. Int. Ed.* **2016**, *55*, 15268-15271.

[31] H. Han, Y. Jiang, S. Zhang, C. Xia, *Phys. Chem. Chem. Phys.* **2023**, *25*, 12629-12640.

[32] a) F. S. Baumann, J. Fleig, H.-U. Habermeier, J. Maier, *Solid State Ionics* **2006**, *177*, 1071-1081; b) V. C. Kournoutis, F. Tietz, S. Bebelis, *Fuel Cells* **2009**, *9*, 852-860; c) L. Almar, J. Szasz, A. Weber, E. Ivers-Tiffee, *J. Electrochem. Soc.* **2017**, *164*, F289-F297; d) A. Leonide, B. Ruger, A. Weber, W. A. Meulenberg, E. Ivers-Tiffee, *J. Electrochem. Soc.* **2010**, *157*, B234-B239; eI. A. Robinson, Y.-L. Huang, S. A. Horlick, M. Hussain, A. Pesaran, E. D. Wachsman, *Electrochim. Acta* **2023**, *442*.

[33] F. Monaco, V. Tezyk, E. Siebert, S. Pylypko, B. Morel, J. Vulliet, T. Le Bihan, F. Lefebvre-Joud, J. Laurencin, *Solid State Ionics* **2018**, *319*, 234-246.

[34] R. Merkle, J. Maier, *Angew. Chem.* **2008**, *47*, 3874-3894.

[35] J. Laurencin, M. Hubert, K. Couturier, T. L. Bihan, P. Cloetens, F. Lefebvre-Joud, E. Siebert, *Electrochim. Acta* **2015**, *174*, 1299-1316.

[36] D. Martin, D. Duprez, *J. Phys. Chem.* **1996**, *100*, 9429-9438.

Entry for the Table of Contents

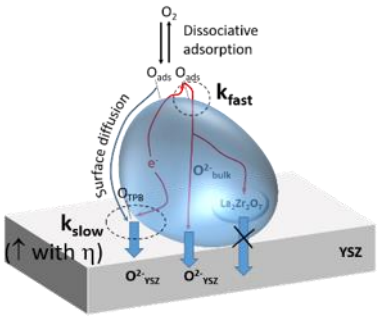

Surface oxygen mobility increased by electrode overvoltage

The multi-step process for oxygen mobility in solid oxide electrolyser cells including dissociation and incorporation in the electrolyte is investigated with polarized oxygen isotopic exchange. The fastest way is O^{2-} incorporation in the electrode catalyst if it shows mixed ionic and electronic properties, whereas the much slower surface path can be activated by the electrode overpotential (η).

Supporting information for:

Influence of Electrode Potential on Oxygen Mobility Probed by Polarized Isotopic Exchange: Insights for Electro-Assisted Oxidation Reactions

Alexandre Manon, Alexandre Nau, Thomas Belin, Arnaud Mazurier, Jean Marc Bassat, Nicolas Bion and Clément Comminges*

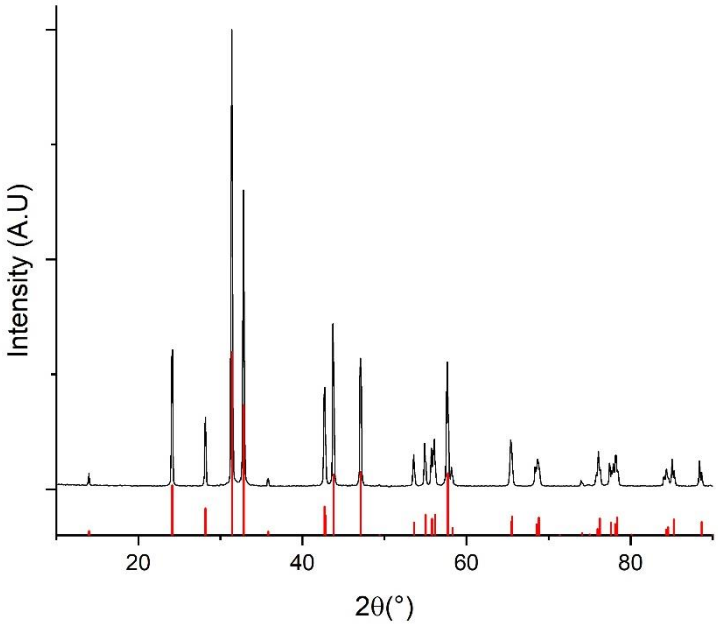

Figure S1: Powder X-ray diffraction at room temperature of synthesised $La_2NiO_{4+\delta}$ and PDF card 01-072-1241.

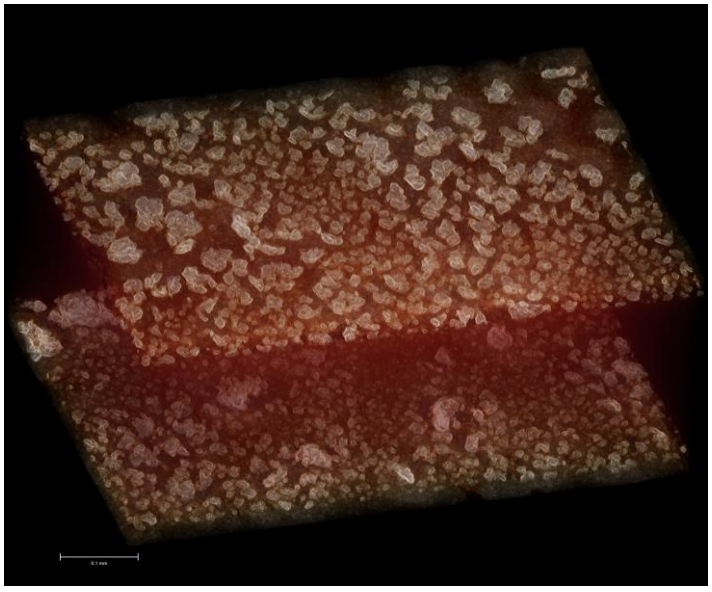

Figure S2: X-ray tomography of the LSM symmetrical cell. Focus on the CGO particles. Scale bar = 0.1 mm.

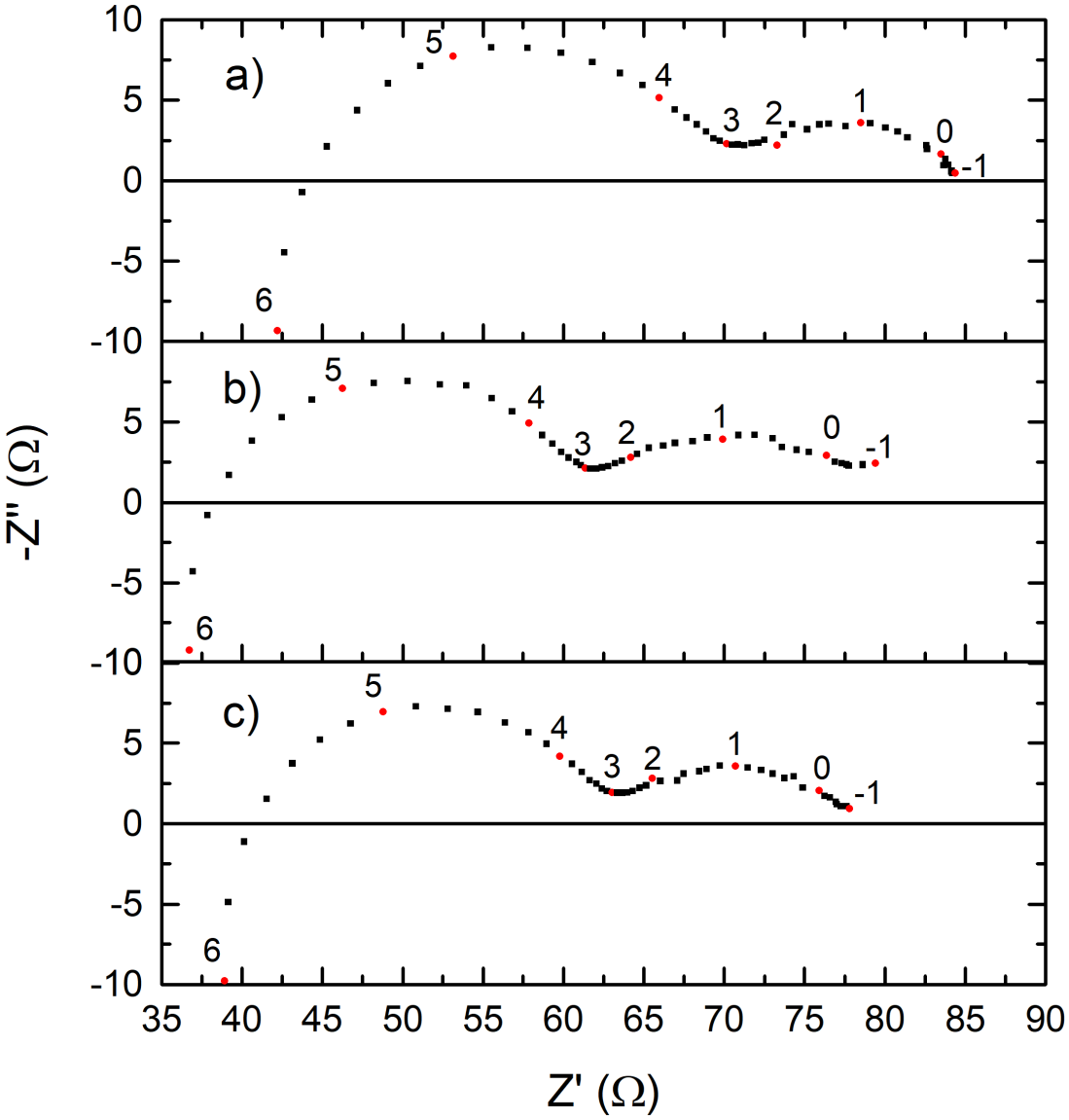

Figure S3: Nyquist plots of the LNO cell at 700°C at OCV, measured before the polarized oxygen isotopic exchange experiments at a) ΔE = 0 V (R_p = 40.6 Ω), b) ΔE = 1 V (R_p = 39.6 Ω) and c) ΔE = 2 V (R_p = 36.7 Ω) with PO_2 = 50 mbar.

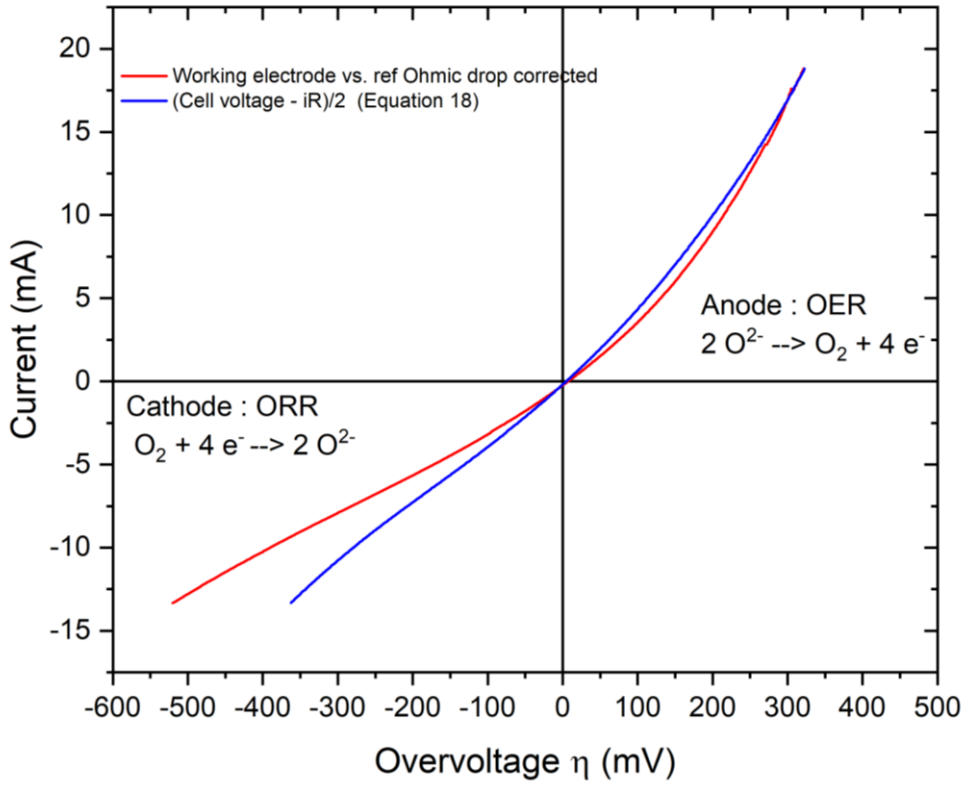

Figure S4: Linear scan voltammetries (20 $mV.s^{-1}$) at 600°C under oxygen flux for a LNO symmetrical cell comprising a Pt ring reference electrode. Working electrode *vs.* reference electrode (red) as well as cell voltage (blue) are plotted as function of overvoltage. Overvoltage was calculated with equation 18 for the cell (blue curve). Overvoltage for the three-electrode configuration is calculated with an ohmic drop correction of the data set (red curve).

The asymetric cell LNO+Pt/YSZ/LNO with a Pt reference electrode was done by applying Pt ink (fuellcellmaterials) on one face of a prepared LNO/YSZ/LNO cell. The Pt ink was applied on the YSZ disk with a PTFE spatula to form a ring with the inside and outside diameters of roughly 19mm and 20 mm respectively on one surface of a prepared LNO/YSZ/LNO cell forming an annular reference electrode around the central LNO working electrode. The LNO+Pt/YSZ/LNO cell with fresh Pt was then heat treated at 900°C for two hours in air. A ring-shaped folded Pt wire placed between the sample holder (alumina tube) and the LNO+Pt face was used as electrical contact for the reference electrode.

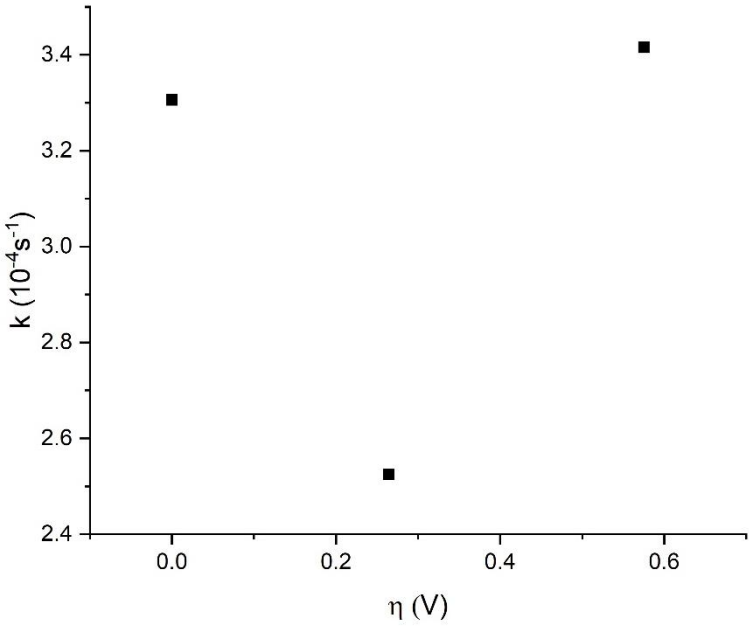

Figure S5: Kinetic constant k (surface path) as a function of applied overvoltage obtained for a second LNO symmetrical cell during POIE at P_{O2} = 50 mbar at 700°C.

Table S1. Electrochemical parameters and kinetic constant k (surface path) determined from equation 20 for LSM symmetrical cell.

T (°C)	ΔE (V)	R_{HF} (Ω)	I (mA)	η (mV)	k (s^{-1})	A (%)	R^2
600	0	14	0	0	2.69E-04	96.8	0.9971
600	0.3	13.84	2.6	132	2.31E-04	97.1	0.9983
600	1.5	12.17	65.79	350	5.47E-04	83.5	0.9525
500	0	27.6	0	0	8.18E-05	99.3	0.9994
500	0.3	27.27	0.335	145	7.88E-05	99.0	0.9990
500	1.5	29.1	19.88	461	2.50E-04	94.6	0.9937
400	0	163.6	0	0	2.03E-05	99.7	0.9969
400	0.3	162.3	0.0245	148	1.83E-05	99.4	0.9965
400	1.5	162	2.08	582	3.95E-05	99.1	0.9967

Table S2. Electrochemical parameters and kinetic constants k_{fast} (bulk path) and k_{slow} (surface path) determined from equation 21 for LSCF symmetrical cell.

T (°C)	ΔE (V)	R_{HF} (Ω)	I (mA)	η (mV)	k_{fast} (s^{-1})	A_{fast} (%)	k_{slow} (s^{-1})	A_{slow} (%)	R^2
600	0	7.25	0	0	1.92E-2	56.7	1.81E-4	43.3	0.9750
600	0.3	7.25	27.0	52.1	1.92E-2	58.9	2.07E-4	41.1	0.9751
600	1.5	7.06	160	185	2.07E-2	63.3	6.47E-4	36.7	0.9869
500	0	19.43	0	0	7.16E-3	52.5	9.68E-5	47.5	0.9943
500	0.3	18.7	4.57	107	6.76E-3	50.1	9.82E-5	49.9	0.9964
500	1.5	18.15	44.9	343	7.11E-3	59.8	2.34E-4	40.3	0.9961
400	0	146.4	0	0	8.59E-4	20.1	6.00E-5	79.9	0.9999
400	0.3	140.2	0.264	132	1.13E-3	19.1	7.04E-5	80.9	0.9993
400	1.5	138.2	4.89	412	7.78E-4	26.4	7.36E-5	73.6	0.9998

Table S3. Electrochemical parameters and kinetic constant k (surface path) determined from equation 20 for LNO symmetrical cell.

T (°C)	ΔE (V)	R_{HF} (Ω)	I (mA)	η (mV)	k (s^{-1})	A (%)	R^2
700	0	62.8	0	0	3.72E-4	99.0	0.9995
700	0.25	45.9	2.57	66	2.23E-4	96.9	0.9956
700	0.5	43.5	4.75	147	1.67E-4	98.4	0.9977
700	2	46.1	27.1	376	2.37E-4	96.2	0.9933
700	3	47	45.4	433	3.62E-4	95.9	0.9947
600	0	72.4	0	0	4.30E-5	95.9	0.9925
600	0.5	67.8	0.837	222	2.48E-5	86.4	0.9750
600	1.2	70.8	4.73	433	4.26E-5	97.6	0.9959
600	1.6	69.3	7.40	544	4.66E-5	97.3	0.9954
600	2	70.8	12.4	561	6.56E-5	96.1	0.9928